Int J Adv Manuf Technol (2017) 89:2077–2085
DOI 10.1007/s00170-016-9246-4

ORIGINAL ARTICLE

# Study on deformation and residual stress of laser welding 316L T-joint using 3D/shell finite element analysis and experiment verification

**Youmin Rong**[1] · **Guojun Zhang**[1] · **Yu Huang**[1]

Received: 4 April 2016 / Accepted: 25 July 2016 / Published online: 6 August 2016
© Springer-Verlag London 2016

**Abstract** In this paper, T-joint of 316L steel is obtained by subsection laser welding method without jig, while a thermal elastic-plastic finite element model considering multi-linear yield stress curves and multi-point constraint equations is developed to estimate welding deformation and residual stress. A simplified heat source model with the actual bead geometry is proposed to reduce the number of finite element meshes. Prediction errors between the simulation and experimental measurement results of angular distortions of three reference lines are −11.0, 0.9, and 7.9 % respectively, and the maximum residual stress is 396 MPa. Meanwhile by microstructure analysis, austenite and ferrite are consisted in weld, segregation and dendritic structures are also observed, while the heat-affected zone is very narrow. In a word, weld line with large travel can be welded by subsection laser welding method without jig, while the finite element method proposed in this paper is effective to predict welding deformation and residual stress.

**Keywords** Welding deformation · Residual stress · Subsection laser welding · Shell/3D FEM · Microstructures

✉ Yu Huang
yuhuang7208@163.com

Youmin Rong
ymrong1987@gmail.com

[1] State Key Lab of Digital Manufacturing Equipment and Technology, School of Mechanical Science and Engineering, Huazhong University of Science and Technology, Wuhan, China

## 1 Introduction

Welding is one of the most important manufacturing processes, but high heating and cooling rates near the fusion zone would induce large welding deformation and residual stress. To reduce and further eliminate the negative influence from the welding deformation and residual stress on the weld quality, it is necessary to accurately predict them before welding.

Currently, the prediction methods mainly include thermal elastic-plastic finite element method (TEP-FEM) and inherent strain analysis (ISA). TEP-FEM is used to predict transient thermal and strain-stress fields. Sun et al. investigated the difference of welding temperature field, welding deformation, and residual stress distribution between laser welding and $CO_2$ gas arc welding [1]. Ikushima et al. applied graphics processing unit to improve the computation efficiency of welding deformation and residual stress, while hardening rules of isotropic hardening, kinematic hardening, and combined hardening of them were also discussed [2]. Considering the heat loss induced by molten metal droplets, Eslampanah et al. proposed a simplified heat source model to simulate residual stress and deformation of T-fillet welded joint [3]. The metallurgical phase transformation behavior was integrated in TEP-FEM to accurately predict residual stress and distortion state of laser welding AA6056 with T-joint [4]. The multi-sequence welding of large-scale structures was analyzed from the point of residual stress and distortion [5]. A thermo-mechanical interface element was introduced by Li et al. to predict welding deformation of stiffened structure [6]. Ma et al. quantitatively revealed the influence principle from jig constraint on longitudinal shrinkage, transverse shrinkage, and angular distortion [7]. The welding deformation in thin-plate bead-on joint

was investigated by means of both experiment and TEP-FEM simulation methods considering external restraint [8]. For gas metal arc welding different steel grades (S355–S960) into T-fillet joints, the influence of thermo-mechanical material properties on welding residual stresses and angular distortion was revealed by Bhatti et al. [9].

Meanwhile, ISA is usually applied to predict welding deformation of large-scale structures while values of inherent strain are directly obtained according to the simulation results of TEP-FEM. Longitudinal inherent shrinkage, transverse inherent shrinkage, longitudinal inherent bending, and transverse inherent bending were calculated with different energy ratios by Ma et al. [10]. Interactive substructure method was applied to TEP-FEM computation, while a database of inherent deformations for eight different materials including 144 computational cases was developed [11]. Interface element formulation was introduced into ISA to predict welding deformation of thin-plate panel structure [12] and the asymmetric curved plate structure [13], while the influences of welding procedure and assembly sequence on the final distortion were examined numerically. Hybrid method of local TEP-FEM with global ISA was built to predict welding deformation of SUS 301 steel with thickness of 1.33 mm [14]. Angular distortion in no gap butt joint was predicted by ISA considering the actual bead geometry [15].

In a word, TEP-FEM is the basis for simulating transient welding behavior and supporting efficient prediction of welding deformation for large structures using ISA. However, TEP-FEM element mesh for simulating laser welding is usually generated small enough to build an accurate heat source, and thus, the computation time would be apparently increased. Meanwhile, laser beam diameter is small, and the beam center is easy to deviate from the welding path because of real-time fluctuation of welding deformation. To study this issue, three aspects would be presented in this paper: (a) a subsection welding method without jig for 316L T-joint is applied to avoid the deviation of beam center; (b) a new heat source model is proposed to reduce the poor effect from the actual laser beam diameter on FEM meshing size; (c) nulti-point constraint equations are developed to couple shell elements with solid elements in order to build shell/3D TEP-FEM and thus short computation time, while multi-linear yield stress curves are applied to improve the model accuracy.

## 2 Experiment

### 2.1 Materials

Base metal is austenite stainless steel 316L with the size of 400 × 200 × 5 mm, and its chemical composition is shown in Table 1 [16]. To protect the welded zone from oil pollution and oxide film disturbing, each contact surface of the welded plates is cleaned by milling process and then wiped clean using acetone before welding.

**Table 1** Chemical composition of 316L (wt.%)

| C | Si | Mn | P | S | Cr | Mo | Ni | N | Cu |
|---|---|---|---|---|---|---|---|---|---|
| 0.021 | 0.77 | 1.019 | 0.039 | 0.001 | 16.92 | 2.03 | 12.16 | 0.033 | 0.20 |

### 2.2 Welding conditions

Figure 1a shows the laser welding system in this study. The laser welding head is installed on the end position of robot ABB IRC5 M2004. The laser beam is acquired by fiber laser IPG YLR-4000. Two plates are welded into T-joint, and the whole welding process is completed without jig. The laser welding head and the sample are both tilted about 45° so as that the laser beam is able to reach the scheduled welding zone. The stiffener and skin plates are fixed by laser spot welding with the power of 3.2 kW before welding. To avoid laser beam center deviation from welding path induced by welding deformation, joining the stiffener plate to skin plate is completed four times. As shown in Fig. 1b, both sides of the stiffener plate are respectively welded with two passes, and the boundary between two adjacent seams is located in the center zone of the whole sample. The welding power is set 4 kW, and defocus length is −2 mm. Welding speed is 0.6 m/min, and flux of argon shielding gas is 0.6 $m^3$/h. Cooling time between the first and second welding stages is 340 s. Time difference from the second pass end to the third pass start is 480 s, while interval between the third pass with the fourth pass remains 480 s. Meanwhile, the whole welding path is planned by the teaching programming method.

### 2.3 Measurement method

In this study, angular distortion, bead geometry, and microstructure are measured respectively. Figure 2 illustrates the measurement method of angular distortion. One side of the skin plate is pressed on the cast iron platform, and angular deformations of lines 1, 2, and 3 (Fig. 1b) are measured by the height vernier caliper. Five points for each line are measured, and interval distance between two adjacent measurement points along the measurement line is 20 mm. Images of the bead geometry and microstructure are obtained using optical microscope. To precisely identify the fusion line between the base metal and the seam, the sample is dissolved in the

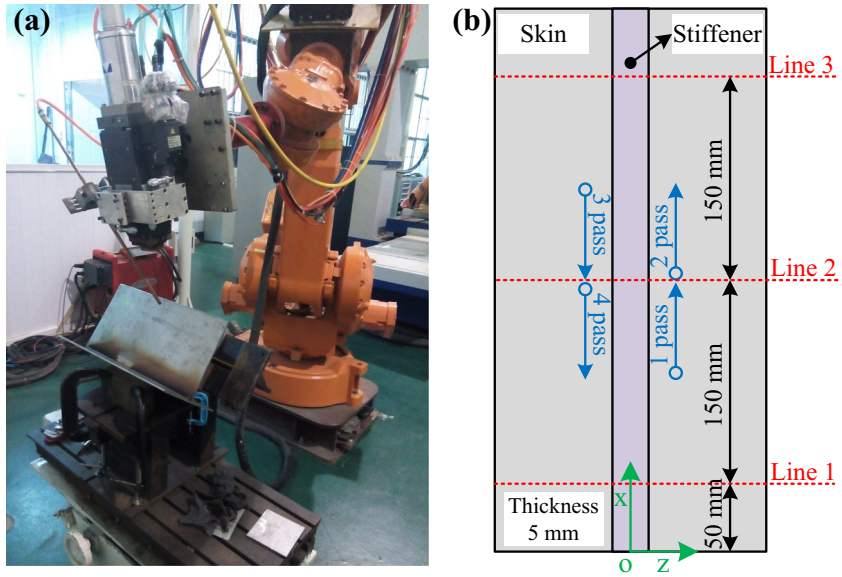


**Fig. 1** Laser welding 316L without jig: **a** system setup and **b** top view of welded sample

aqua regia that is compounded by hydrochloric acid and nitric acid with the volume ratio of 3:1. It is noted that microstructures of the fusion zone are analyzed with the magnification of 200, 500, and even 800. In addition, the size of bead geometry is measured by CSM1 software.

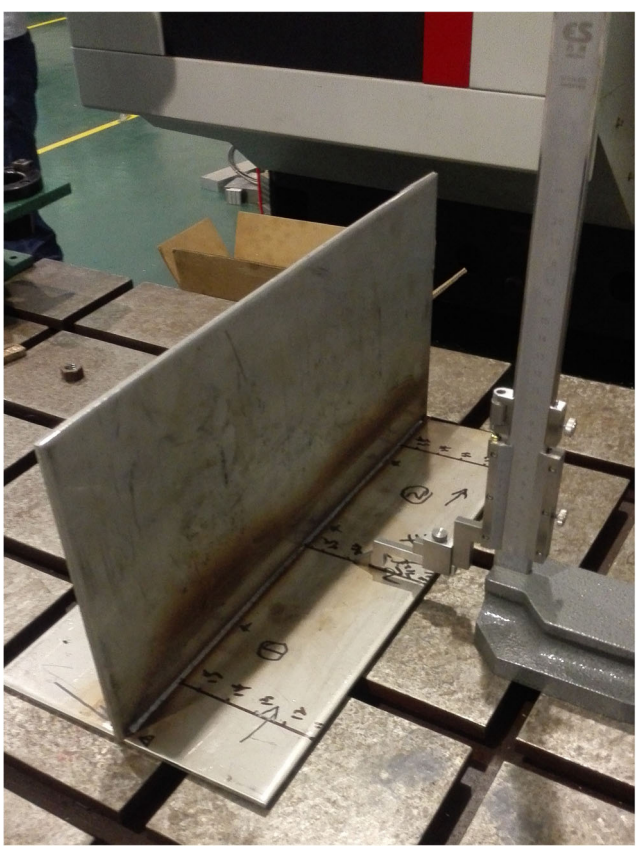

**Fig. 2** Measurement method of angular distortion

## 3 Numerical theory

### 3.1 Thermal model

In heat transfer analysis, the transient temperature field would be computed according to Fourier's thermal conducting equation (Eq. ((1))).

$$\rho(T)c_p(T)\frac{\partial T}{\partial t} = \lambda(T)\left[\frac{\partial}{\partial x}\left(\frac{\partial T}{\partial x}\right)+\frac{\partial}{\partial y}\left(\frac{\partial T}{\partial y}\right)+\frac{\partial}{\partial z}\left(\frac{\partial T}{\partial z}\right)\right]+Q_L \quad (1)$$

where $\rho(T)$ represents density, $\lambda(T)$ is thermal conductivity, $c_p(T)$ expresses specific heat capacity, and $Q_L$notes the heat source distribution. Meanwhile, a novel heat source model considering the actual bead profile is proposed in this paper, as shown in Eq. ((2)).

$$Q_L = \frac{\eta P_L}{A_c L_s} \quad (2)$$

where $\eta = 0.80$ is the efficiency of laser welding, $P_L = 4.0$KW means the total laser power, $A_c$ represents the cross-sectional area of the bead, and $L_s$ expresses the simulation step size along the welding direction. It is noted that the computation model would be more really react the welding process by inducing the actual bead shape to the heat source. The initial

temperature is assumed as 25 °C. During welding process, heat loss by convection and radiation is simplified by heat transfer coefficient $h_c$ [17].

$$h_c = \begin{cases} 0.0668T & \mathrm{W}/\left(m^2 \cdot {}^oC\right) \quad T < 500^oC \\ 0.231T - 82.1 & \mathrm{W}/\left(m^2 \cdot {}^oC\right) \quad T \geq 500^oC \end{cases} \tag{3}$$

### 3.2 Mechanical model

In welding process, the initial strain is assumed to be induced by temperature field. The material stress state can be expressed as Eq. ((4)) [18].

$$d\boldsymbol{\sigma} = \boldsymbol{D}d\varepsilon - \boldsymbol{C}dT \tag{4}$$

where **D** is elastic matrix or plastic matrix and **C** is temperature-stress matrix. The material yield criterion is proposed as Eq. (5).

$$f(\boldsymbol{\sigma}) = f_0\left(\varepsilon_p, T\right) \tag{5}$$

where yield function is $f$ and yield stress function $f_0$ is related to temperature and plastic strain. According to plastic flow rule, plastic strain increment can be expressed as Eq. ((6)).

$$d\varepsilon_p = \lambda \frac{\partial f}{\partial \boldsymbol{\sigma}} \tag{6}$$

where $\lambda$ is a positive value of scalar. Two unknown matrixes in Eq. ((4)) are calculated by Eqs. ((7)), ((8)), and ((9)) [19].

$$\boldsymbol{D} = \boldsymbol{D}_p = \boldsymbol{D}_e - \boldsymbol{D}_e \frac{\partial f}{\partial \boldsymbol{\sigma}} \frac{\partial f}{\partial \boldsymbol{\sigma}^T} \boldsymbol{D}_e / \boldsymbol{S} \tag{7}$$

$$\boldsymbol{C} = \boldsymbol{C}_p = \boldsymbol{D}_P \left( \alpha + \frac{\partial \boldsymbol{D}_e^{-1}}{\partial T} \boldsymbol{\sigma} \right) - \boldsymbol{D}_e \frac{\partial f}{\partial \boldsymbol{\sigma}} \frac{\partial f_0}{\partial T} / \boldsymbol{S} \tag{8}$$

$$\boldsymbol{S} = \frac{\partial f}{\partial \boldsymbol{\sigma}^T} \boldsymbol{D}_e \frac{\partial f}{\partial \boldsymbol{\sigma}} + \frac{\partial f_0}{\partial \varepsilon_p^T} \frac{\partial f}{\partial \boldsymbol{\sigma}} \tag{9}$$

where $\alpha$ is a linear expansion coefficient. It is necessary to note that the material elastic state can be presented if ignoring yield function $f$. Furthermore, the equilibrium state (Eq. (10)) of each element is established according to the principle of virtual displacement.

$$d\boldsymbol{F}^e + \int \boldsymbol{B}^T \boldsymbol{C} \mathrm{dTdV} = \int \boldsymbol{B}^T \boldsymbol{D} \boldsymbol{B} d\boldsymbol{\delta}^e dV \tag{10}$$

For welding simulation, $d\boldsymbol{F}^e = 0$means load increment of each node for each element. **B** represents relationship matrix between strain and displacement. $d\boldsymbol{\delta}^e$ is the displacement increment of each node. Eventually, transient deformation and residual stress of the welded sample can be computed by integrating calculation results of all elements.

### 3.3 Computation procedure

Numerical simulation process is completed using secondary development function of ANSYS. Computing hardware platform is Windows 64-bit system, Intel (R) Core (TM) i7-4790K, CPU 4.00 GHz, RAM 32 GB. According to the chemical component as shown in Table 1, temperature-dependent physical properties of 316L steel are plotted in Fig. 3. Multi-linear yield strength curves related to different strains and temperatures are developed to display a more complex plasticity flow state, because yield stress is different while strain is changed. In a high-temperature zone, young's modulus and yield strength are set to small constants in order to guarantee the simulation convergence.

The geometry model, including shell and solid (shell/3D) parts, is built and meshed. Width values of solid part in skin and stiffener plates are both 40 mm, and the rest of the parts are all developed as the shell model. Figure 4 shows the mesh distribution of shell/3D model. The distance between node 353 and node 357 is two computation step sizes (5.3 mm). SOLID 70 elements and SHELL 131 elements are applied in thermal analysis, while SOLID 185 elements and SHELL 181

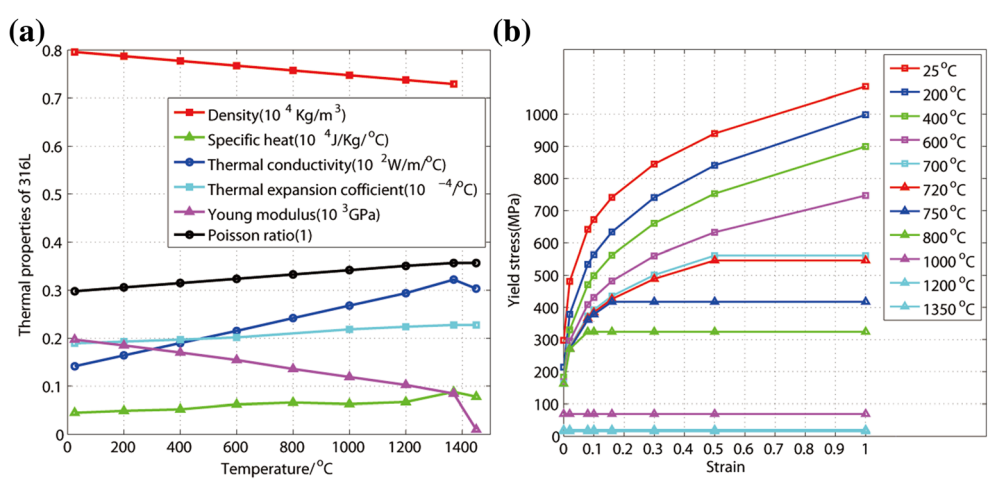


**Fig. 3** Material physical parameters of **a** thermo-physical and mechanical properties, **b** yield strength curves related to different strains and temperatures

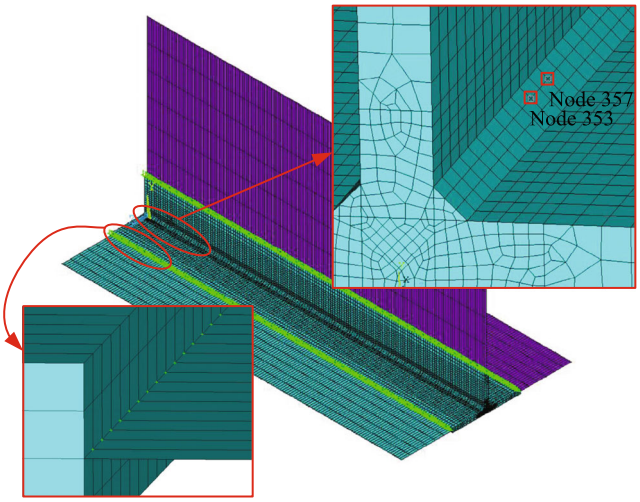


**Fig. 4** Mesh generation of shell/3D model

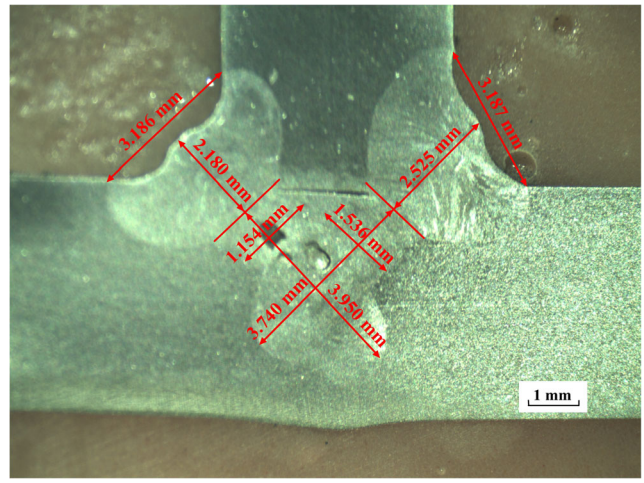


**Fig. 5** T-joint bead geometry of laser welding 316L steel

elements with six degrees of freedom (DOF) per node are used in mechanical analysis. Kinematic hardening rule of material is considered in mechanical analysis. To join solid elements with shell elements, multi-point constraint formulation (Eq. ((11))) is proposed. The relationship between the solid node and the shell node is decided by constraint coefficients. It is necessary to emphasize that the number of elements and nodes would be reduced and further simulation efficiency can also be improved. The whole shell/3D model consists of 59,553 elements, which corresponds to 65,833 DOF. To avoid rigid movement, four vertex points of skin plate are respectively fixed as 3 DOF, 1 DOF, 2 DOF, and 1 DOF, while the rotation DOFs are free.

$$\text{Cons} = \sum_{i=1}^{n} [a(i) \times U(i)] \tag{11}$$

where Cons means a constant, $U(i)$ represents DOF, and $a(i)$ is constraint coefficient for the $i$th node.

## 4 Results and discussion

### 4.1 Metallographic structure analysis

The microstructure of the T-joint weld by laser welding is shown in Fig. 5. Three obvious porosity defects appear at the junction of two seams. To be convenient to build 3D model considering the actual bead geometry, the weld cross section is simplified as a combination shape of trapezoid and rectangle, and thus the weld area $A_c$ in Eq. ((2)) can be calculated as 10.77 mm$^2$. As shown in Fig. 6a, the microstructures of the base metal near the fusion line remain equiaxed austenite grains. It is found from Fig. 6b that the base metal grains near the fusion line do not grow clearly and the heat-affected zone (HAZ) is narrow, while the second phase is not observed. The same structure has also been found in austenitic steel [16, 20]. Figure 7a illustrates the distinct microstructure growth direction at the center of seam zone. Near the central region of the weld, segregation (Fig. 7b) is induced by the non-spontaneous nucleation particle that refines grains. During laser welding 316L, metallographic structures of austenite and ferrite are precipitated. Comparing the microstructures in Fig. 6c and Fig. 7c, it is observed that austenite content is higher near the weld center than that around the fusion line.

### 4.2 Thermal analysis

The comparison result of the cross-section between the actual weld and the simulation shape is given in Fig. 8a. A good agreement is observed between the experiment and numerical results. Figure 8b illustrates two time history curves of node 353 and node 357 that are noted in Fig. 4. The starting temperature before the laser beam arrived is 25 °C. The peak temperatures of both nodes 353 and 357 are 2408.3 and 2446.2 °C, respectively. Obviously, computation step size $L_s$ (2.65 mm) along welding direction is reasonable because temperature fluctuation near the weld center can be accepted. Figure 8c gives temperature distribution at 340 s after the beginning of the laser welding process. At this moment, the sample is in the cooling state; after that, the first welding stage is completed. Temperature field ranges from 25 to 131.07 °C. Therefore, it is viable that a simplified heat source is proposed considering the actual weld width and depth of penetration.

### 4.3 Mechanical analysis

Mechanical results are computed and obtained under the temperature load. Figure 9 gives the numerical results of angular distortion and residual stress after sufficient cooling. As shown in Fig. 9a, angular distortion is between −1.772 and

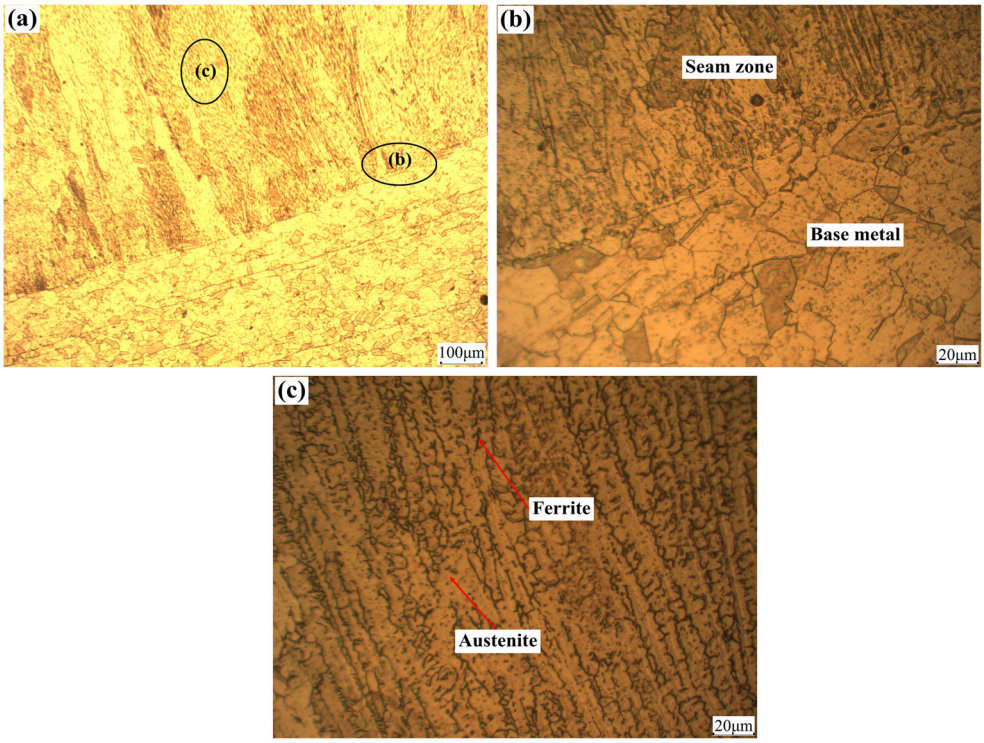


**Fig. 6** Fusion line: **a** magnified 100 times, **b** magnified 500 times, and **c** seam microstructure near the fusion line

0.145 mm. Minimum displacement locates on the outer edge of the skin plate because deformation is restricted by the four fixed vertices. Meanwhile, maximum displacement presents on the stiffener plate that is drew by the inclined fusion zone.

The final residual stress distribution is presented in Fig. 9b. Distributions of residual stress for every subsection welding are similar with each other. Maximum residual stress (396 MPa) mainly appears at the start and end positions of each welding stage. Near the adjacent position between the first pass and the second pass, an obvious reduction of residual stress (about 180 MPa) along the welded seam center appeared in the second pass side.

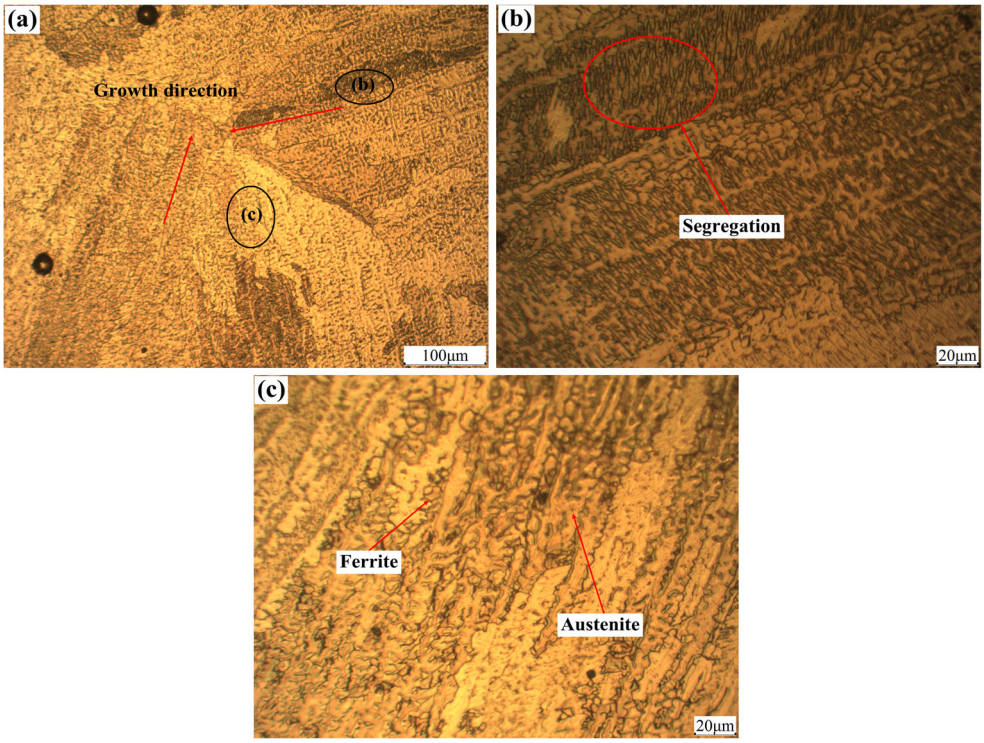


**Fig. 7** Grain growth: **a** the middle position of weld, **b** segregation zone in the seam center and **c** magnified 500 times of crystal growth directions

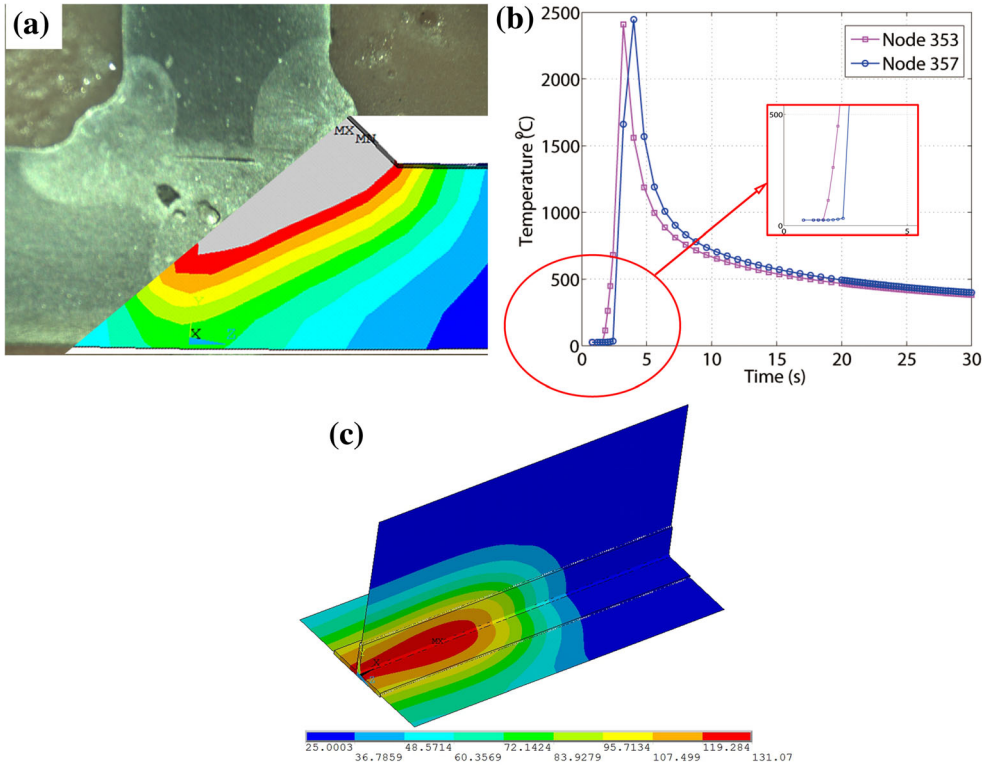


**Fig. 8** Simulation results of **a** bead profile compared with the experiment, **b** time history of two node temperatures along welding direction, and **c** temperature field distribution 340 s after the beginning of the welding process

To further demonstrate TEP-FEM correctness, the angular distortions and residual stresses in the welding direction (along line 1, line 2, and line 3, seen in Fig. 1b) on the upper surface of the skin plate are presented in Fig. 10. As shown in Fig. 10a to Fig. 10c, maximum angular deformations measured by height vernier caliper (Fig. 2) along three lines are 3.00, 3.24, and 3.66 mm, respectively, while these results acquired by TEP-FEM are 3.33, 3.21, and 3.37 mm in turn. According to the calculating formula of the relative error (RE) [21], values of RE are −11.0, 0.9, and 7.9 %. The errors may be caused by the measurement method of the experiment result and the model simplification of TEP-FEM. Tendency of angular distortion for line 1 and line 3 are similar. It should be stated that measurement results of one side of the welded seam center are all zero because this side is compressed and fixed. And thus, angular distortions measured in this paper are the double of the actual deformations.

Longitudinal residual stresses of three reference lines are plotted in Fig. 10d, and the maximum residual stress is around 350 MPa. The tensile stresses at the weld line reach the yield strength of the 316L steel, which then decrease to zero, finally become compressive state at the surface of the skin plate far from weld line. Meanwhile, the fluctuation of longitudinal residual stress of line 1 and line 3 keeps a similar tendency. The tendency of the compressive stresses of line 2 is apparently different with that of line 1 and line 3, while maximum compressive stress is 157.94 MPa. The distribution of residual stress for line 2 obtained by subsection laser welding is obviously different with that of the published articles [22–25]. It is concluded that this phenomenon is caused by weld junction between the end position of this subsection welding stage and the start zone of the next subsection welding stage. Therefore, the proposed model, by integrating multi-linear yield stress curves and multi-point constraints to TEP-FEM, is used to

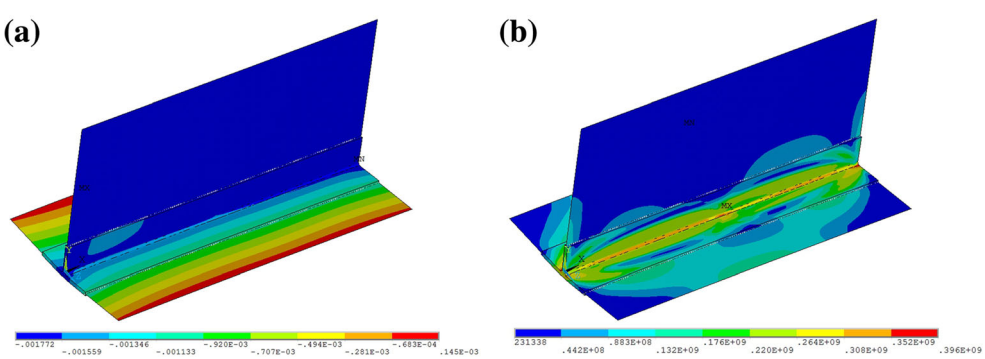


**Fig. 9** Simulation results of **a** angular distortion and **b** residual stress

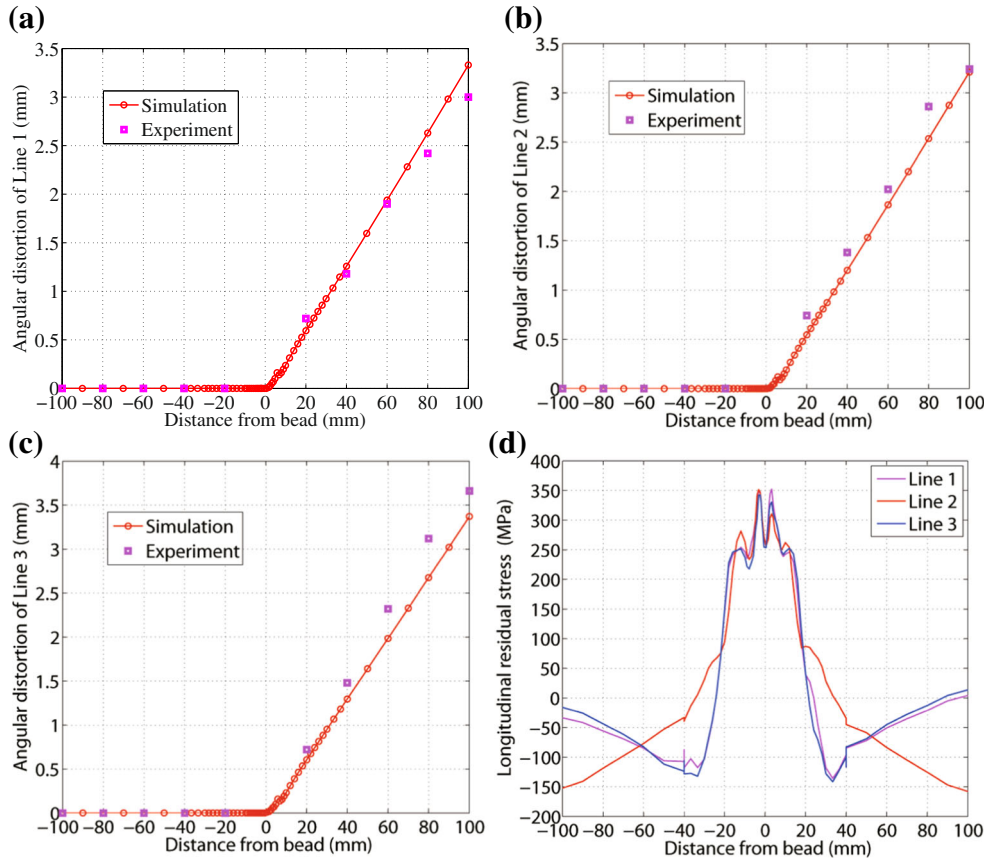


**Fig. 10** Comparison results of welding deformation along **a** line 1 in Fig. 1b, **b** line 2 in Fig. 1b, **c** line 3 in Fig. 1b, and **d** longitudinal residual stresses along three reference lines

guide how welding deformation and residual stress can be decreased in the actual laser welding process.

## 5 Conclusions

In the presented research, T-joint of 316L steel is obtained by subsection laser welding method without jig, while TEP-FEM based on ANSYS code is developed to estimate welding deformation and residual stress. Comparing the computation results with the verification experiment, three conclusions can be drawn.

(1). Weld path with long travel can be welded by subsection laser welding method without jig. By microstructure analysis, austenite and ferrite are consisted in weld, segregation and dendritic structures are also observed, while the HAZ is very narrow.

(2). Considering multi-linear yield stress curves and multi-point constraint method, a TEP-FEM considering multi-linear yield stress curves and multi-point constraint equations is built. Meanwhile, a simplified heat source considering the actual bead geometry is proposed to reduce the number of finite element meshes.

(3). The prediction errors between the simulation and experimental measurement results of angular distortions for three measured lines are −11.0 %, 0.9 % and 7.9 % respectively, and the maximum residual stress is 396 MPa.

Therefore, the proposed simulation model can be applied to predict welding deformation and residual stress and further supply input data for ISA in order to further guide the actual laser welding process.

**Acknowledgment** This research is supported by the National Basic Research Program of China (973 Program, NO.2014CB046703) and the Fundamental Research Funds for the Central Universities (HUST: 2016YXMS271). The authors also express their gratitude to engineer Xiyuan Hu and postgraduate Zeyang Zhao for their help in experiment process.

## References

1. Sun J, Liu X, Tong Y, Deng D (2014) A comparative study on welding temperature fields, residual stress distributions and deformations induced by laser beam welding and $CO_2$ gas arc welding. Mater Des 63:519–530
2. Ikushima K, Itoh S, Shibahara M (2015) Development of idealized explicit FEM using GPU parallelization and its application to large-

scale analysis of residual stress of multi-pass welded pipe joint. Weld World 59:589–595
3. Eslampanah AH, Aalami-aleagha ME, Feli S, Ghaderi MR (2015) 3-D numerical evaluation of residual stress and deformation due welding process using simplified heat source models. J Mech Sci Technol 29(1):341–348
4. Zain-ul-abdein M, Nelias D, Jullien JF, Boitout F, Discher L, Noe X (2011) Finite element analysis of metallurgical phase transformations in AA 6 056-T4 and their effects upon the residual stress and distortion states of a laser welded T-joint. Int J Pressure Vessels Pip 88:45–56
5. Keivani R, Jahazi M, Pham T, Khodabandeh AR, Afshar MR (2014) Predicting residual stresses and distortion during multi sequence welding of large size structures using FEM. Int J Adv Manuf Technol 73:409–419
6. Li Y, Wang K, Jin Y, Xu M, Lu H (2015) Prediction of welding deformation in stiffened structure by introducing thermo-mechanical interface element. J Mater Process Technol 216:440–446
7. Ma N, Huang H, Murakawa H (2015) Effect of jig constraint position and pitch on welding deformation. J Mater Process Technol 221:154–162
8. Deng D, Liu XZ, He J, Liang W (2016) Investigating the influence of external restraint on welding distortion in thin-plate bead-on joint by means of numerical simulation and experiment. Int J Adv Manuf Technol. doi:10.1007/s00170-015-7413-7
9. Bhatti AA, Barsoum Z, Murakawa H, Barsoum I (2015) Influence of thermo-mechanical material properties of different steel grades on welding residual stresses and angular distortion. Mater Des 65: 878–889
10. Ma N, Li L, Huang H, Chang S, Murakawa H (2015) Residual stresses in laser-arc hybrid welded butt-joint with different energy ratios. J Mater Process Technol 220:36–45
11. Wang R, Zhang J, Serizawa H, Murakawa H (2009) Study of welding inherent deformations in thin plates based on finite element analysis using interactive substructure method. Mater Des 30: 3474–3481
12. Deng D, Murakawa H, Ma N (2012) Predicting welding deformation in thin plate panel structure by means of inherent strain and interface element. Sci Technol Weld Join 17(1):13–21
13. Deng D, Murakawa H, Liang W (2008) Prediction of welding distortion in a curved plate structure by means of elastic finite element method. J Mater Process Technol 203:252–266
14. Huang H, Wang J, Li L, Ma N (2016) Prediction of laser welding induced deformation in thin sheets by efficient numerical modeling. J Mater Process Technol 227:117–128
15. Rong YM, Huang Y, Zhang GJ, Chang Y, Shao XY (2016) Prediction of angular distortion in no gap butt joint using BPNN and inherent strain considering the actual bead geometry. Int J Adv Manuf Technol. doi:10.1007/s00170-015-8102-2
16. Feng Y, Luo Z, Liu Z, Li Y, Luo Y, Huang Y (2015) Keyhole gas tungsten arc welding of AISI 316 L stainless steel. Mater Des 85: 24–31
17. Brickstad B, Josefson BL (1998) A parametric study of residual stresses in multi-pass butt-welded stainless steel pipes. Int J Pressure Vessels Pip 75:1l–25
18. Ueda Y, Yamakawa T (1971) Analysis of thermal elastic-plastic stress and strain during welding by finite element method. Trans Jpn Weld Soc 2(2):90–100
19. Wang J (2003) Welding numerical simulation technology and its application (in Chinese). Shanghai Jiao Tong University Press, Shanghai, pp. 89–90
20. Kchaou Y, Haddar N, Henaff G, Pelosin V, Elleuch K (2014) Microstructural, compositional and mechanical investigation of shielded metal arc welding (SMAW) welded super austenitic UNS N08028 (alloy 28) stainless steel. Mater Des 63:278–285
21. Rong YM, Zhou Q, Huang Y, Chang Y, Zhang GJ, Shao XY (2015) Multi-objective optimization of laser brazing with the crimping joint using ANN and NSGA-II. Int J Adv Manuf Technol. doi:10.1007/s00170-015-8028-8
22. Mondal AK, Biswas P, Bag S (2015) Influence of tacking sequence on residual stress and distortion of single sided fillet submerged arc welded joint. J Marine Sci Appl 14:250–260
23. Fu G, Lourenco MI, Duan M, Estefe SF (2014) Effect of boundary conditions on residual stress and distortion in T-joint welds. J Constr Steel Res 102:121–135
24. Peric M, Tonkovic Z, Rodic A, Surjak M, Garasic I, Boras I, Svaic S (2014) Numerical analysis and experimental investigation of welding residual stresses and distortions in a T-joint fillet weld. Mat Des 53:1052–1063
25. Michaleris P, Zhang L, Bhide SR, Marugabandhu P (2006) Evaluation of 2D, 3D and applied plastic strain methods for predicting buckling welding distortion and residual stress. Sci Technol Weld Join 11(6):707–716